2005

Assimilation of Simulated Float Data in Lagrangian Coordinates

J. L. Mead
Boise State University

Assimilation of Simulated Float Data in Lagrangian Coordinates

J.L. Mead *
Department of Mathematics, Boise State University, Boise, ID 83725-1555 USA

February 3, 2004

Abstract

We implement an approach for the accurate assimilation of Lagrangian data into regional general ocean circulation models. The forward model is expressed in Lagrangian coordinates and simulated float data are incorporated into the model via four dimensional variational data assimilation. We show that forward solutions computed in Lagrangian coordinates are reliable for time periods of up to 100 days with phase speeds of 1 m/s and deformation radius of 35 km. The position and depth of simulated floats are assimilated into the viscous, Lagrangian shallow water equations. The weights for the errors in the model and data are varied and the assimilation results react appropriately. We show the effect of different spatial and temporal samplings of float data on all Lagrangian trajectories in the computational domain. At the end of the assimilation period, results from the Lagrangian shallow water equations could be interpolated and used as initial and boundary conditions in an Eulerian general ocean circulation model.

Keywords: Lagrangian methods, data assimilation, shallow water equations

1 Introduction

A vast amount of data are collected from floats and drifters in the ocean. For example, in 2002, the international ARGO project has approximately 550 floats in the global ocean, with the ultimate goal of having 3000 floats collecting temperature, salinity and velocity measurements. The project includes drifters that remain at the surface and continuously transmit data to ARGO satellites, and near-surface drifters that transmit their data every few days. In addition, there are sub-surface floats such as ALACE and RAFOS floats. ALACE floats repeatedly surface,

*E-mail address: jmead@boisestate.edu

while RAFOS floats surface only at the end of their deployment. Data from these floats and drifters are all recorded in a Lagrangian reference frame.

These Lagrangian data enhance existing observing systems by expanding spatial and temporal coverage, however, the ocean is still underrepresented. General circulation models can fill in the gaps, but there are uncertainties in these models so taking observations directly into them produces poor quality forecasts, even though data represent the 'true' state of ocean circulation within measurement errors.

Data assimilation is a way to accurately extract information from observations, and combine them with a model that contains information about dynamical processes and their interactions. In this work variational assimilation is applied to simulated float data and the viscous, shallow water equations in Lagrangian coordinates.

There are two major difficulties associated with assimilating Lagrangian data into regional general circulation models, and using Lagrangian coordinates remedies them both. The first problem is that most models are written in Eulerian coordinates, and Lagrangian data must be interpolated to a fixed grid, which introduces new errors in the data. In addition, nonlinear measurement functionals must be used for data assimilation.

The second problem is that uniqueness of solutions and continuous dependence upon inputs of the primitive equations in an open ocean domain is not guaranteed [13]. The problem arises whenever the particle speeds lie within the range of the phase speeds of the hydrostatic internal gravity waves. Different boundary conditions must be applied when the flow is subcritical with respect to the graver, faster modes versus when the flow is supercritical with respect to the higher, slower modes. In numerical models appropriate boundary conditions can be specified point wise in the vertical direction, but this is not practical. Alternatively, it was shown by Bennett and Chua [2] that uniqueness of solutions can be guaranteed in the open ocean if the domain moves with the flow. In a comoving domain, vorticity is conserved on fluid particles, and it cannot advect into or out of the domain. Divergence can radiate into or out of the domain as gravity wave propagation, thus every mode is subcritical in the reference frame of the moving boundary. The result is that in the vertical, the boundary conditions do not need to be applied mode by mode in a comoving domain.

Lagrangian coordinates are not the only way to have boundaries that move with the flow in an open domain. Popular front tracking methods such as the level set method [14] and volume of fluid [12] do not resolve the ill-posedness of the primitive equations in the open ocean because these methods use an Eulerian domain, and a moving boundary is only tracked. On the other hand, unified coordinates [17] is an interesting approach because it can be Eulerian, Lagrangian

or somewhere in between depending on the choice of a parameter. The authors suggest that a purely Lagrangian domain is not a good choice, and they suggest following 'pseudo-particles' which are somewhat slower than particles that move with the flow. Again, in this instance the ill-posedness in the open ocean is not resolved since the domain does not move with the flow, but at a slower speed. The arbitrary Lagrangian Eulerian method, (ALE) [9], temporarily computes in a domain that moves with the flow but at some arbitrary point in time, the domain is re-gridded and becomes Eulerian. If one chooses to re-grid the domain at nearly every time-step, the approach is then semi-Lagrangian [15], which is a method often used in atmospheric models to allow longer time steps for integration.

In this work, we choose to use Lagrangian coordinates and follow floats (or particles) in a purely Lagrangian manner. This allows us to ensure uniqueness of solutions and continuous dependence upon inputs of the primitive equation model in the open ocean, allows linear measurement functionals for data assimilation, and results in a well posed inverse problem. In [10] we tested the feasibility of this approach, and we are able to assimilate simulated data into the inviscid shallow water equations in Lagrangian coordinates for a few hours. Here, we add friction to the model and show more extensive results for much longer time periods.

Difficulties with assimilating data into a model written in Lagrangian coordinates parallel difficulties that arise when collecting data from floats or drifters in the ocean. One is that the particles in the model (or floats and drifters) may clump together in areas with a lot of activity leaving some areas void. However, this situation may be advantageous because the majority of the data or information from the model are in areas with the majority of the activity. Obtaining more information in areas with the majority of the activity is often sought numerically by using adaptive mesh refinement [3]. Another difficulty with using Lagrangian coordinates is that the model is highly nonlinear. As shown in Section 2, we find that in the open ocean, the flow can be simulated for over 3 months. This not only allows the Lagrangian shallow water equations to be used for simulation of near-surface and mid-ocean floats which have integral time scales of days and weeks, but also deep-ocean floats which have time scales of months. Lastly, Lagrangian motion exhibits chaos in the sense that if one drops two floats in (virtually) the same location, they can have drastically different trajectories. We also find that solutions of the Lagrangian model can be different depending on the initial conditions or choice of numerical method.

Lagrangian data have been combined with Eulerian models in [8, 11, 16]. In [16] they do a quantitative comparison of Eulerian velocity fields from the 24-level Primitive Ocean Model (POM) with drogued drifter position data using geometric orthogonal functions. They use this spectral approach to reconstruct Eulerian velocity fields with sparse Lagrangian data. They

demonstrate that trajectories yielded from the Eulerian velocity fields with sparse Lagrangian data are more accurate than those yielded from the model velocity fields.

In [8] they use variational data assimilation to combine an Eulerian reduced gravity model with drifting buoys. They minimize a cost functional which measures the distance between model simulated drifters and observed drifters, with the Eulerian model added as a strong contraint. In addition, they treat the mean upper layer thickness as a parameter in the optimzation process. Their main results include finding an optimal upper layer thickness so that the model can fit the data. In this work, we also show through variational data assimilation that the model can fit the data. However, we accomplish this not by treating upper layer thickness as a parameter, but by minimzing a cost function that not only measures the distance between model simulated floats and observed drifters, but in addition minimizes the weighted error in the model and initial conditions.

More recently, in [11] they use optimal interpolation to combine an Eulerian velocity field from a quasi-geostrophic model with Lagrangian data. There, they quantify the effectiveness of assimilating Lagrangian data by showing that the optimal time interval between measurements is 5-15 hours for drifters at the surface, and 1.5-2 days for the subsurface.

In Section 2 we derive the Lagrangian form of the viscid, shallow water equations in spherical polar coordinates on a flat earth. In Section 3 we define linear Picard iterations on the model and show that they can be used to approximate the solution of the nonlinear model. In Section 4 we formulate the inverse model and assimilate data for 13 days. In Section 5 we give conclusions.

2 Lagrangian Shallow Water Model

2.1 Formulation of the Model

The primitive equations are commonly used for general ocean circulation, however, we will use a prototype for the primitive equations: the shallow water equations. Essentially, the shallow water equations are one layer of the primitive equations that follow a surface of constant density.

In an Eulerian domain, the inviscid shallow water equations in spherical coordinates are

$$\frac{Du}{Dt} = \frac{uv}{r}\tan\theta + fv - \frac{g}{r\cos\theta}\frac{\partial h}{\partial\lambda} \tag{1}$$

$$\frac{Dv}{Dt} = -\frac{u^2}{r}\tan\theta - fu - \frac{g}{r}\frac{\partial h}{\partial\theta} \tag{2}$$

and the corresponding continuity equation is

$$\frac{\partial h}{\partial t} + \frac{1}{r\cos\theta}\left(\frac{\partial}{\partial\lambda}(hu) + \frac{\partial}{\partial\theta}(hv\cos\theta)\right). \tag{3}$$

The longitude is λ, the latitude is θ, u is the velocity in the Eastern direction, v is the velocity in the Northern direction, h is the depth over a flat bottom, f is the Coriolis parameter, r is the radius of the earth, and g is the gravitational acceleration.

Regardless of the coordinate system, $\frac{D\boldsymbol{u}}{Dt}$ (with $\boldsymbol{u} = [u \;\; v]$) denotes differentiation following the motion of the fluid. In Eulerian coordinates

$$\frac{D\boldsymbol{u}}{Dt} = \frac{\partial \boldsymbol{u}}{\partial t} + \boldsymbol{u} \cdot \nabla \boldsymbol{u},$$

and we solve the shallow water equations for $u(\lambda, \theta, t)$, $v(\lambda, \theta, t)$, and $h(\lambda, \theta, t)$ at time t where the latitude λ, and longitude θ are fixed.

In Lagrangian coordinates

$$\frac{D\boldsymbol{u}}{Dt} = \frac{\partial \boldsymbol{u}}{\partial t},$$

which is a much simpler expression for advection of momentum. However, the pressure gradient term (i.e. the right hand side of (1)-(2)) becomes highly nonlinear. In order to write (1)-(3) in Lagrangian coordinates, consider that the velocity of a particle (or float) is solely a function of its initial position. Denote the initial longitude and latitude of a particle by α and β respectively, and its subsequent longitude by $\lambda(\alpha, \beta, t)$, latitude by $\theta(\alpha, \beta, t)$, and depth by $h(\alpha, \beta, t)$. To convert from Eulerian coordinates $u(\lambda, \theta, t), v(\lambda, \theta, t)$, and $h(\lambda, \theta, t)$ to Lagrangian coordinates $\lambda(\alpha, \beta, t), \theta(\alpha, \beta, t)$, and $h(\alpha, \beta, t)$ use the identities

$$u = r\cos\theta \frac{\partial \lambda}{\partial t}, \qquad v = r\frac{\partial \theta}{\partial t}. \tag{4}$$

The momentum equations for the shallow water model in Lagrangian coordinates are

$$\frac{\partial^2 \lambda}{\partial t^2} = 2\tan(\theta)\frac{\partial \lambda}{\partial t}\frac{\partial \theta}{\partial t} + \frac{f}{\cos\theta}\frac{\partial \theta}{\partial t} - \frac{g}{r^2\cos^2\theta} J^{-1}\left(\frac{\partial h}{\partial \alpha}\frac{\partial \theta}{\partial \beta} - \frac{\partial \theta}{\partial \alpha}\frac{\partial h}{\partial \beta}\right) \tag{5}$$

$$\frac{\partial^2 \theta}{\partial t^2} = -\sin(\theta)\cos(\theta)\left(\frac{\partial \lambda}{\partial t}\right)^2 - f\cos(\theta)\frac{\partial \lambda}{\partial t} - \frac{g}{r^2} J^{-1}\left(\frac{\partial \lambda}{\partial \alpha}\frac{\partial h}{\partial \beta} - \frac{\partial h}{\partial \alpha}\frac{\partial \lambda}{\partial \beta}\right) \tag{6}$$

where the Jacobi determinant is

$$J \equiv \frac{\partial(\lambda, \theta)}{\partial(\alpha, \beta)},$$

with the notation

$$\frac{\partial(\dagger, \ddagger)}{\partial(\alpha, \beta)} \equiv \frac{\partial \dagger}{\partial \alpha}\frac{\partial \ddagger}{\partial \beta} - \frac{\partial \ddagger}{\partial \alpha}\frac{\partial \dagger}{\partial \beta}.$$

The continuity equation (3) in Lagrangian coordinates takes on a simpler form:

$$\frac{\partial}{\partial t}(h\cos\theta J) = 0, \tag{7}$$

which can be integrated exactly.

Given the particles' initial positions α, β, initial velocities u, v and initial depths h, with appropriate boundary conditions (see below), we solve the Lagrangian shallow water model (5)-(7) for the particles' position $\lambda(\alpha,\beta,t)$ $\theta(\alpha,\beta,t)$ and depth $h(\alpha,\beta,t)$ at time t. Solutions in Lagrangian coordinates are illustrated here by plotting $(\lambda(\alpha_i,\beta_j,t),\theta(\alpha_i,\beta_j,t))$ for all t, i.e. by plotting one or more of the particles' trajectories in the computational domain with initial positions (α_i,β_j).

Boundary conditions that result in a well-posed initial boundary value problem for the inviscid Lagrangian shallow water model are specification of (i) the longitude λ at the East and West boundaries, (ii) the latitude θ at the North and South boundaries, and (iii) the depth h at all four boundaries [2]. Even though there is a complete mathematical understanding of the initial boundary value problem in an open domain, the numerical implementation of these boundary conditions is a challenge. These boundaries are artificial because general ocean circulation continues across and beyond these open boundaries. In order accommodate information trying to leave the domain absorbing or non-reflecting boundary conditions must be used to ensure that the information is not reflected back into the domain at the artificial interface [6]. In long integrations the Lagrangian shallow water equations are more sensitive to these reflections than the Eulerian form, due to their highly nonlinear form. In addition, the exact solution of the test problem used here is unknown, so boundary values are only a rough approximation and may be quite different from values in the interior. This makes reflections even worse. Future work will address absorbing boundary conditions for the Lagrangian shallow water equations.

In these experiments we use periodic boundary conditions which will give us a good understanding of Lagrangian solutions in the interior of the domain. Periodic boundary conditions in an open domain necessitate modeling on a flat Earth. This is a reasonable assumption for the region modeled here, since the domain is not that large. Let θ_0 be the southern-most value of θ in the domain of interest, then the change in coordinates (4) simplifies to

$$u = r\cos\theta_0 \frac{d\lambda}{dt}, \qquad v = r\frac{d\theta}{dt}.$$

Adding friction to the momentum equations for the shallow water model in Eulerian coordinates only amounts to adding $\kappa\nabla^2 u$ to (1) and $\kappa\nabla^2 v$ to (2) where κ is the viscosity coefficient. In Lagrangian coordinates friction is not as straightforward, but on a flat Earth it is possible to use the full Lagrangian form. The viscous term added to (5) is

$$\kappa r\cos\theta_0 \left\{ \frac{1}{r^2\cos^2\theta_0} J^{-1}\frac{\partial(L,\theta)}{\partial(\alpha,\beta)} + \frac{1}{r^2} J^{-1}\frac{\partial(\lambda,M)}{\partial(\alpha,\beta)} \right\}, \tag{8}$$

while the viscous term added to (6) is

$$\kappa r \left\{ \frac{1}{r^2 \cos^2\theta_0} J^{-1} \frac{\partial(N,\theta)}{\partial(\alpha,\beta)} + \frac{1}{r^2} J^{-1} \frac{\partial(\lambda,O)}{\partial(\alpha,\beta)} \right\}, \tag{9}$$

with

$$L = J^{-1} \frac{\partial\left(\frac{\partial\lambda}{\partial t},\theta\right)}{\partial(\alpha,\beta)} \quad M = J^{-1} \frac{\partial\left(\lambda,\frac{\partial\lambda}{\partial t}\right)}{\partial(\alpha,\beta)}$$
$$N = J^{-1} \frac{\partial\left(\frac{\partial\theta}{\partial t},\theta\right)}{\partial(\alpha,\beta)} \quad O = J^{-1} \frac{\partial\left(\lambda,\frac{\partial\theta}{\partial t}\right)}{\partial(\alpha,\beta)}.$$

2.2 Numerical Results from the Forward Viscid Lagrangian Shallow Water Model

We choose to model a region in the North Atlantic extending from from 38° North to 40° North and from 38° West to 40° West. In this region, the deformation radius is approximately 35 km, and phase speeds c are 1 m/s [4]. The test problem has initial conditions which are a combination of plane waves of small amplitude, or Sverdrup waves [7]. This combination solves the linear form of (1)-(3) exactly, and is given by

$$u = -2\sin(l\theta - \omega t + M)\frac{g\hat{H}}{\omega^2 - f^2}\left[\frac{k}{r\cos\theta}\omega\sin(k\lambda + L) + \frac{l}{r}f\cos(k\lambda + L)\right] \tag{10}$$

$$v = 2\cos(l\theta - \omega t + M)\frac{g\hat{H}}{\omega^2 - f^2}\left[\frac{l}{r}\omega\cos(k\lambda + L) + \frac{k}{r\cos\theta}f\sin(k\lambda + L)\right] \tag{11}$$

$$h = H + 2\cos(k\lambda + L)\cos(l\theta - \omega t + M)\hat{H}, \tag{12}$$

$$\omega^2 = f^2 + c^2\left[\left(\frac{k}{r\cos\theta}\right)^2 + \left(\frac{l}{r}\right)^2\right].$$

Here $H = c^2/g$ is the mean depth, $\hat{H} = \epsilon H$, $\epsilon = 0.01$, and $f = 2\Omega\sin\theta$ is the Coriolis parameter. Since the deformation radius is 35 km, the longitudinal and latitudinal wave numbers are $k = l = 180$ per radian of longitude and latitude. In addition, to have spatially periodic initial conditions in the interval of interest $L = 40\pi$ and $M = -38\pi$. Lastly, the viscosity coefficient κ in (8) and (9) was chosen so that the grid Reynolds number is equal to 1, i.e.

$$\kappa = \triangle\alpha\epsilon c.$$

Forward model experiments were run with second order finite differences in space and time for 100 days. The grid spacing is 0.083°, with 24×24 particles in the domain, and constant time steps of 75 seconds. The depths of the particles remain fairly constant at approximately

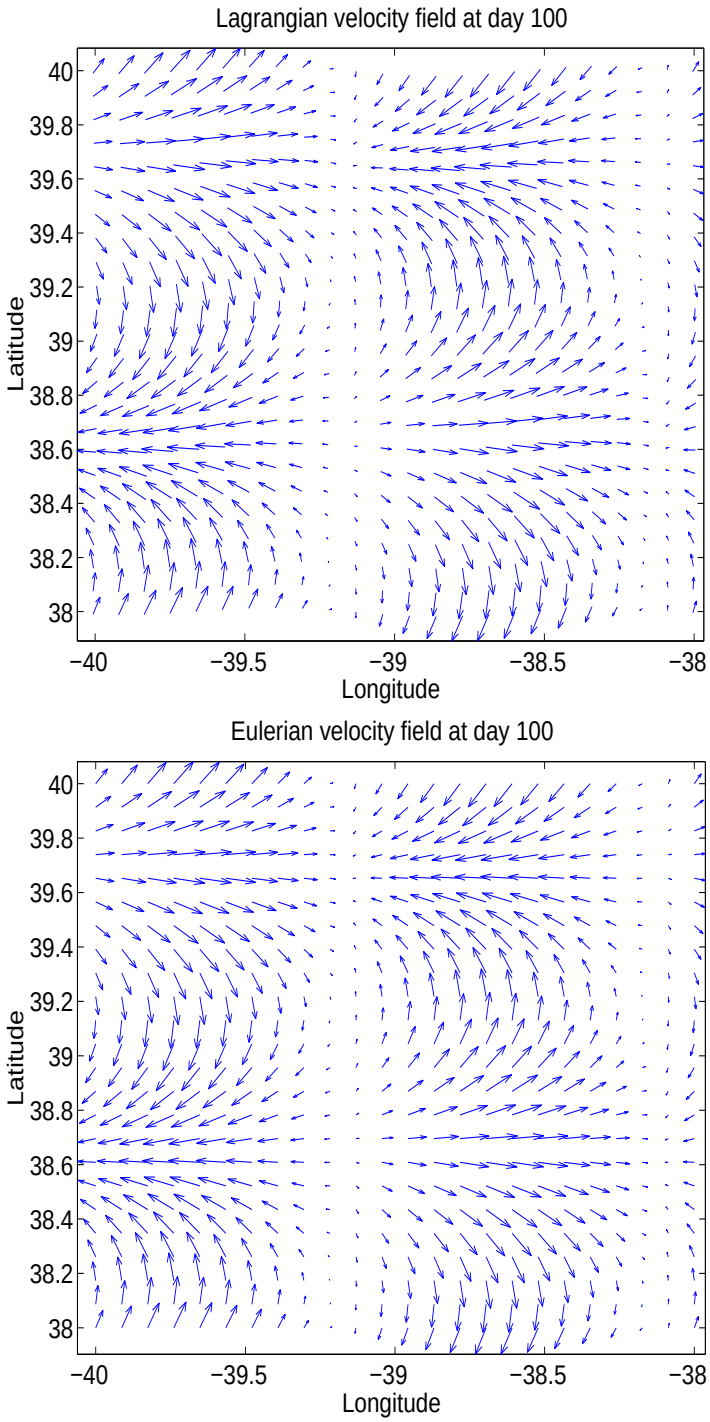

Figure 1: Lagrangian velocity field (top) and Eulerian velocity field (bottom) at day 100.

0.10 m, so graphs of h are not shown here. The solution of the viscous Eulerian shallow water equations was also computed in the same manner to validate the Lagrangian results.

The particle positions at day 100, calculated by the viscous Lagrangian shallow water equations, are used to calculate velocities on a Lagrangian grid and this velocity field is shown in Figure 1. For comparison, the Eulerian velocity field at day 100 is also shown in Figure 1, and it is seen by inspection that the flow is very similar to that in the the Lagrangian vector field. The reliability of the solution on the Lagrangian grid at day 100 is further validated in Figure 2 where the three dimensional plot of the meridional and zonal velocities from the Lagrangian and Eulerian calculations at day 100 are shown. The velocities from both methods at day 100 are uniformly smooth between 0.1 and -0.1 m/s.

Figures 1 and 2 are the usual way to view Eulerian solutions, but here we are interested in Lagrangian solutions. Typically, the entire history of Lagrangian data are plotted as trajectories, contrary to the vector field where only information at day 100 is plotted. Thus in Figures 3 and 4 we plot the 100 day trajectory solution from the Lagrangian shallow water equations. These Figures are more detailed displays of the Lagrangian results in Figures 1 and 2. In Figure 3 the solution at all 24×24 grid points, i.e. on all 24×24 particles, is plotted and we see a correlation to the vector field in Figure 1. Figure 4 is a closer view of the trajectories in Figure 3. By looking more closely at the particles in Figure 4, we see that with the given initial conditions, the particles are oscillating, drifting north, with the radius of their oscillations increasing.

Figures 1-4 show that stable solutions of the Lagrangian shallow water equations in this region can be found for time periods of at least 100 days. Even though the scales here are correct, without more realistic initial conditions we will not have realistic trajectory solutions from the forward Lagrangian shallow water model. Thus in the following sections we describe the process of using the Lagrangian shallow water equation to assimilate Lagrangian data. When real data are used, this process can help give us realistic initial and boundary conditions for general ocean circulation models.

3 Tangent Linear Model

Variational data assimilation, as described in [5], requires a linear forward model. We use the tangent linear model, linearized about a previous iterate, and iterate it to get a nonlinear approximation of the original model. In Appendix A this approach is first illustrated with the Eulerian nonlinear one dimensional wave equation, and then the corresponding linear form for the Lagrangian shallow water model is given.

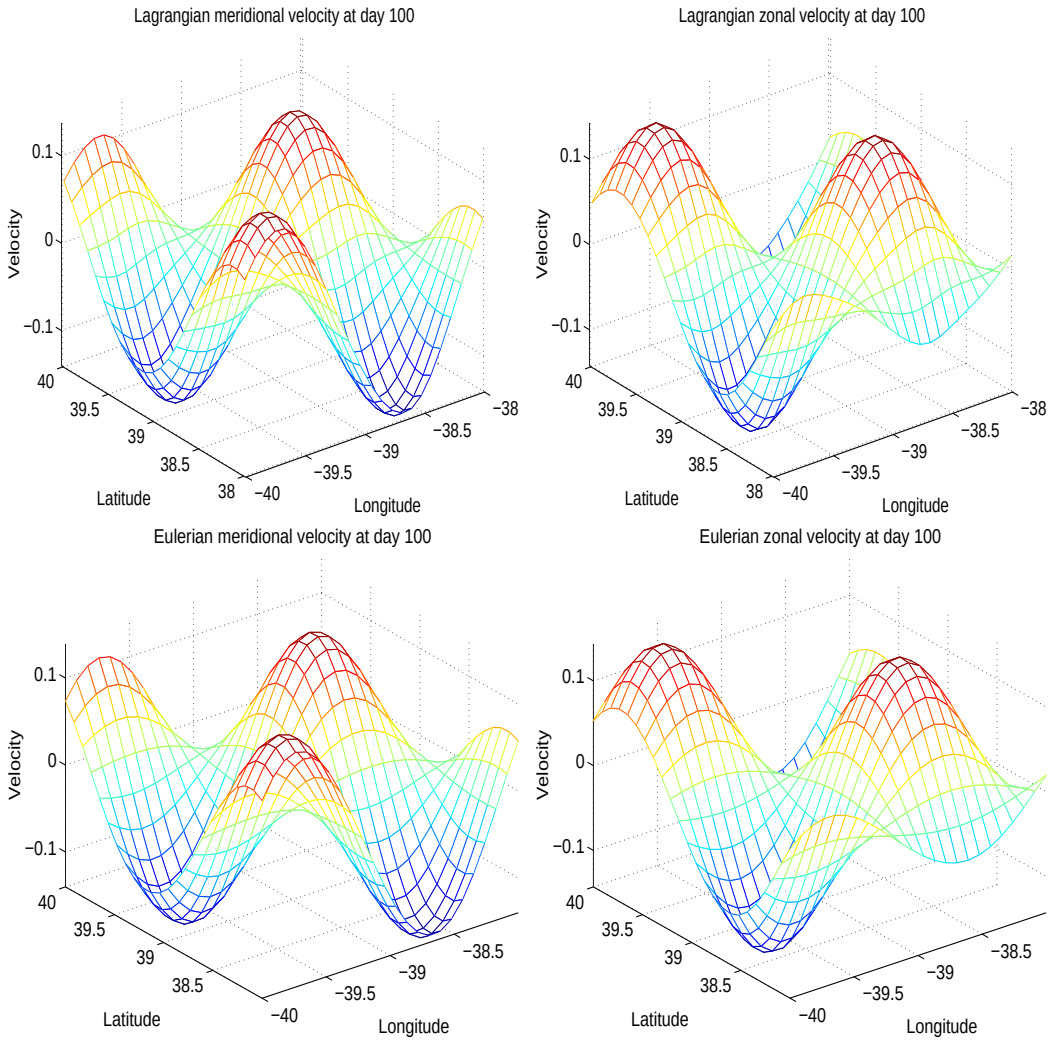

Figure 2: Meridional and zonal velocities on the Lagrangian (top) and Eulerian (bottom) grids at day 100

.

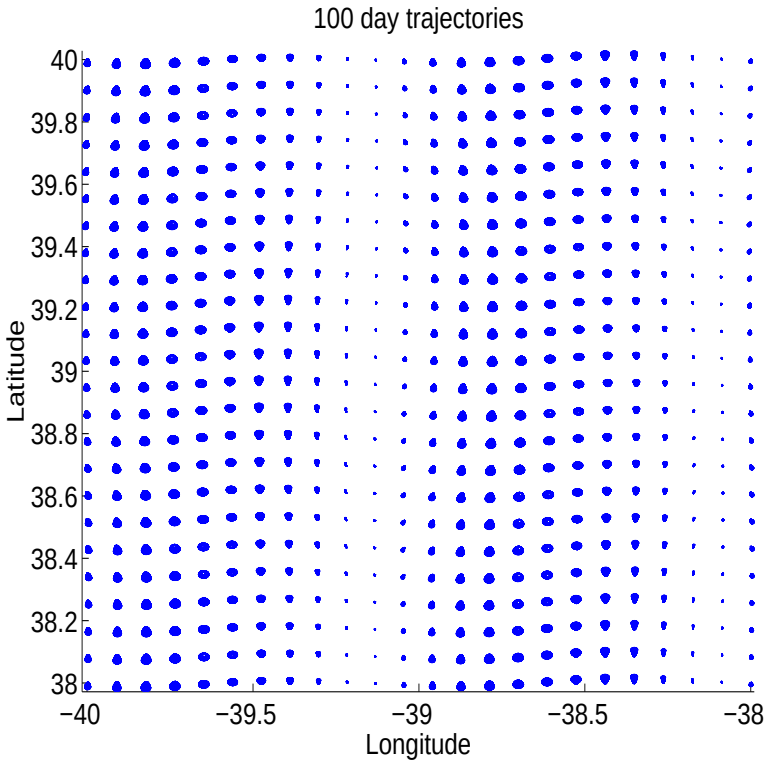

Figure 3: 100 day trajectories of 24 x 24 floats from forward model.

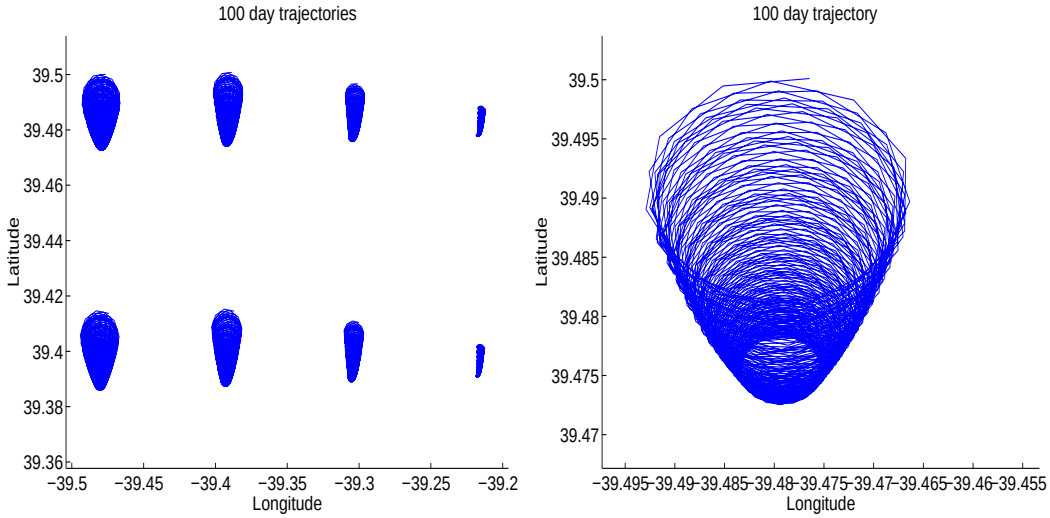

Figure 4: 100 day trajectories of 8 floats (left) and 1 float (right) in Figure 3.

The computational cost of calculating the Lagrangian tangent linear form versus the Eulerian tangent linear form can be estimated by counting the number of dependent vairables in equations (28)-(30) given in Appendix A, versus the number of dependent variables in the Eulerian tangent linear form. In the Lagrangian form as i, j, and p range in (28)-(30) (and if we neglect the zero coefficients) there are 27 dependent variables while in the Eulerian form there are 12 dependent variables. Thus the Lagrangian form is more than twice as expensive as the Eulerian form.

Iterated solutions of the tangent linear form of the Lagrangian shallow water equations are shown in Figure 5. The same initial conditions, (10)-(12), and periodic boundary conditions that were used in the nonlinear experiments were also used here. However, the grid spacing was increased to 0.50° and time steps to 220 seconds, resulting in 4 x 4 particles in the region. This smaller grid was used in order to make these idealized experiments run in a reasonable amount of time.

The nonlinear solution and the initial guess used as the zeroth iterate to start the iterations on the tangent linear form differ in two ways:

1. The initial values of the position and depth differ by 0.04%.

2. The initial velocities differ by 2.0% in both the meridional and zonal directions.

Figure 5 shows the 25 day trajectories of four of the 4 x 4 particles. Plotted there for each trajectory are the initial guesses used to start the tangent linear model (28)-(30) (i.e. the zeroth iterate), the nonlinear (or 'true') trajectories, and the 2nd iterate. We see that the linear model solution converges to the nonlinear model solution exactly after two iterations. The difference between the nonlinear solution, and the second iteration of the linear model is negligible. The behavior of these four particles is characteristic of the remaining particles in the domain.

4 Inverse Lagrangian Shallow Water Model

A detailed description of the data assimilation method can be found in [5]. In Appendix C we describe in detail the formulation of the adjoint model using the notation in Appendix A.

The data assimilation method involves combining the linear model (28)-(30) with the following simulated float data from the ocean

$$\begin{aligned} d_m^\lambda &= \lambda(\alpha_m, \beta_m, t_m) \\ d_m^\theta &= \theta(\alpha_m, \beta_m, t_m) \\ d_m^h &= h(\alpha_m, \beta_m, t_m) \end{aligned}$$

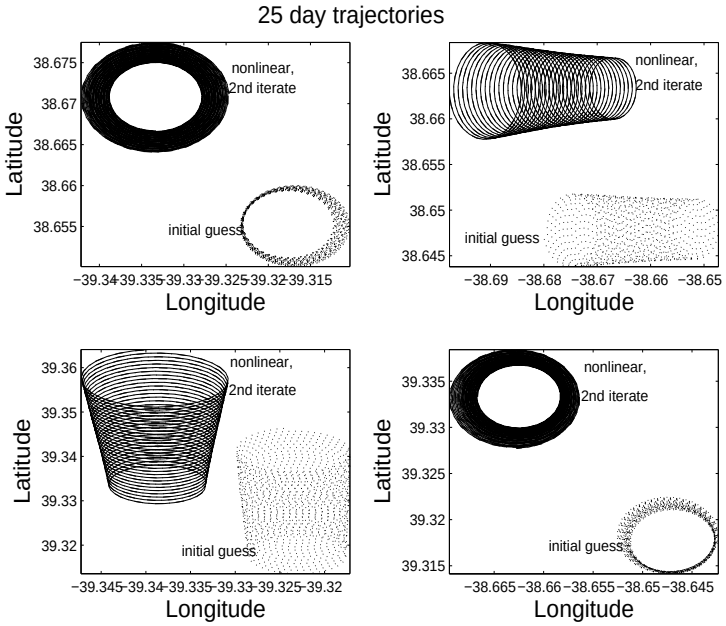

Figure 5: 25 day trajectories of four of the 16 particles in the computational domain: the nonlinear solution, initial guess and 2nd iterate.

where $m = 1, \ldots, K$ and there are $3K$ data. For example, if we monitor two floats, recording their position and depth twice a day for two days $K = 8$, and there are $M = 24$ pieces of data.

It is assumed that the model, initial conditions, and data all contain error and we denote these errors by $f(\lambda, \theta, t)$, $i(\lambda, \theta)$, and $\epsilon(\lambda, \theta, t)$, respectively. Adding appropriate subscripts, this implies the forward model is

$$\frac{\partial^2 \lambda^n}{\partial t^2} = \sum_{i=0}^{2}\sum_{j=0}^{2}\sum_{p=0}^{1}\left(k_{ijp}^{n-1}\frac{\partial^{(i+j+p)}}{\partial\alpha^i\beta^j t^p}\lambda^n + l_{ijp}^{n-1}\frac{\partial^{(i+j+p)}}{\partial\alpha^i\beta^j t^p}\theta^n + m_{ij}^{n-1}\frac{\partial^{(i+j)}}{\partial\alpha^i\beta^j}h^n\right) + c_\lambda^{n-1} + f_\lambda^n \quad (13)$$

$$\frac{\partial^2 \theta^n}{\partial t^2} = \sum_{i=0}^{2}\sum_{j=0}^{2}\sum_{p=0}^{1}\left(\hat{k}_{ijp}^{n-1}\frac{\partial^{(i+j+p)}}{\partial\alpha^i\beta^j t^p}\lambda^n + \hat{l}_{ijp}^{n-1}\frac{\partial^{(i+j+p)}}{\partial\alpha^i\beta^j t^p}\theta^n + \hat{m}_{ij}^{n-1}\frac{\partial^{(i+j)}}{\partial\alpha^i\beta^j}h^n\right) + c_\theta^{n-1} + f_\theta^n \quad (14)$$

$$h^n = \sum_{i=0}^{1}\sum_{j=0}^{1}\left(\bar{k}_{ij}^{n-1}\frac{\partial^{(i+j)}}{\partial\alpha^i\beta^j}\lambda^n + \bar{l}_{ij}^{n-1}\frac{\partial^{(i+j)}}{\partial\alpha^i\beta^j}\theta^n\right) + c_h^{n-1}. \quad (15)$$

Since we replaced J^{-1} with a term proportional to h (found by solving the continuity equation exactly), we have assumed that there is no error in the equation for h. The initial conditions

are

$$\lambda^n(\alpha,\beta,0) = \alpha + i^n_\lambda, \quad \frac{\partial\lambda}{\partial t} = \frac{u^I}{r\cos\theta_0} + i^n_{\lambda_t} \tag{16}$$

$$\theta^n(\alpha,\beta,0) = \beta + i^n_\theta, \quad \frac{\partial\theta}{\partial t} = \frac{v^I}{r\cos\theta_0} + i^n_{\theta_t} \tag{17}$$

$$h^n(\alpha,\beta,0) = h^I, \tag{18}$$

and we will use u^I, v^I, and h^I given in (10)-(12). Lastly, the boundary conditions are periodic, and the data with error are

$$d^\lambda_m = \lambda^n(\alpha_m,\beta_m,t_m) + \epsilon^{\lambda^n}_m \tag{19}$$

$$d^\theta_m = \theta^n(\alpha_m,\beta_m,t_m) + \epsilon^{\theta^n}_m \tag{20}$$

$$d^h_m = h^n(\alpha_m,\beta_m,t_m) + \epsilon^{h^n}_m . \tag{21}$$

In order to find the best fit of the model and data we hypothesize that the circulation fields satisfy (13)-(21) within errors having specified covariances $W^{-1}_{f_\lambda}$, $W^{-1}_{f_\theta}$, $W^{-1}_{i_\lambda}$, $W^{-1}_{i_\theta}$, $W^{-1}_{i_{\lambda_t}}$, $W^{-1}_{i_{\theta_t}}$, ω^{-1}_λ, ω^{-1}_θ, and ω^{-1}_h. The values for these covariances will be discussed in the section describing the twin experiments. Now the best fit of the dynamics (13)-(18) and the data (19)-(21) is found by minimizing the following penalty functional that describes the discrepancy between them:

$$\begin{aligned}
\mathcal{J} = & \int_0^T dt \int_{\alpha_w}^{\alpha_e} d\alpha \int_{\beta_s}^{\beta_n} d\beta \left\{ W_{f_\lambda}(f^n_\lambda)^2 + W_{f_\theta}(f^n_\theta)^2 \right\} \\
& + \int_{\alpha_w}^{\alpha_e} d\alpha \int_{\beta_s}^{\beta_n} d\beta \left\{ W_{i_\lambda}(i^n_\lambda)^2 + W_{i_\theta}(i^n_\theta)^2 + W_{i_{\lambda_t}}(i^n_{\lambda_t})^2 + W_{i_{\theta_t}}(i^n_{\theta_t})^2 \right\} \\
& + \sum_{m=1}^{M} \left\{ \omega_\lambda(\epsilon^{\lambda^n}_m)^2 + \omega_\theta(\epsilon^{\theta^n}_m)^2 + \omega_h(\epsilon^{h^n}_m)^2 \right\} .
\end{aligned}$$

The equation for h, (15), is added to $\mathcal{J}$ as a strong constraint since we assumed (7) was exact in the tangent linear approximation.

The calculus of variations is used to minimize $\mathcal{J}$, and to find the best fit to the dynamics and the data. The result of using the calculus of variations is the Euler-Lagrange equations: a coupled two-point initial boundary value problem consisting of a set of backward and forward equations, and they are given in Appendix C. The Euler-Lagrange equations are decoupled by using the representer method, and the the details can be found in [1].

The notation in Appendices A-C allows straightforward calculation of the continuous adjoint equations from the tangent linear model. One only needs to determine the coefficients of

the tangent linearization (13)-(15) for the particular model of interest and the Euler-Lagrange equations will always be given by (31)-(43).

4.1 Twin Experiments

In this section we give results from identical twin experiments. In these experiments the Lagrangian shallow water model (13)-(18) is used to generate the Lagrangian data d_m^λ, d_m^θ, and d_m^h. Then, under different conditions, this data is assimilated back into the Lagrangian shallow water model. The best fit of the model and data is $\hat{\lambda}$, $\hat{\theta}$, $\hat{h}$ and it is found by solving the Euler-Lagrange equations (31)-(43) with the representer method [1].

We will determine in these twin experiments if the simulated Lagrangian data can be reconciled with the Lagrangian shallow water model. This will be done by investigating the choice of weights on the errors in the model, initial condition, and simulated float data. If we choose a "large" weight on the model errors and a "small" weight on the data errors we would expect the assimilated trajectories to roughly follow the data. This is the situations studied in experiment 1. If the situation were reversed, i.e. a "small" weight on the model errors and a "large" weight on the data errors we would expect the assimilated trajectories to roughly behave as the forward model predicts. This is the situation in experiment 2.

We will also study the effects of different spatial and temporal sampling of data. If the spatial sampling is sparse we must rely heavily on the model. In experiment 1, however, we specified "large" weights on the errors in the model and sparse spatial sampling. We would expect, and we verify, that the trajectories where there are no data give poor representations of the true ocean when the data is sparse and the model error is large. Thus if we specify large errors in the model, the spatial sampling should be dense. On the other hand, if the spatial sampling is sparse, we must rely heavily on the model and specify small model error.

Optimal temporal samplings are given in [11]. Here we do not find optimal strategies with the Lagrangian shallow water model, rather, we study the relationship between different spatial and temporal sampling strategies.

In the twin experiments the same grid spacing, initial and boundary conditions, and numerical methods used in the forward and tangent linear model experiments were used here. In addition, the initial guess and the true ocean differ in the same two ways that the initial guess and nonlinear solution differ in the tangent linear experiments. That is,

1. The initial values of the position and depth differ by 0.04%.

2. The initial velocities differ by 2.0% in both the meridional and zonal directions.

4.2 Choice of Weights

The values for the weights on the dynamics, initial conditions and data are the inverse of the covariances of the errors in the dynamics, initial conditions and data. The error covariance matrices are diagonal, and constant, with values $\sigma^2 I$ (although more dense matrices that reflect correlated errors can be used). The standard deviation of the errors σ were estimated in the following manner:

- The standard deviation of the initial position and velocity errors are a specified percentage of the average position and velocity, respectively. The values used for the averages are $|\theta| = |\lambda| \approx .741765d0$ radians, and $\left|\frac{\partial \lambda}{\partial t}\right| = \left|\frac{\partial \theta}{\partial t}\right| \approx \frac{u}{r} \approx \frac{\epsilon c}{r} \approx \frac{1 \times 10^{-3}}{6 \times 10^6} \approx 2 \times 10^{-9}$ radians/second ($\sim 1 \times 10^{-2}$ m/s).
- The standard deviation of the model errors are a specified percentage of the average accelerations. The values used for the averages are $\left|\frac{\partial^2 \lambda}{\partial t^2}\right| = \left|\frac{\partial^2 \theta}{\partial t^2}\right| \approx \frac{fu}{r} \approx 1 \times 10^{-4} \frac{1 \times 10^{-3}}{6 \times 10^6} \approx 2 \times 10^{-13}$ radians/second^2 ($\sim 1 \times 10^{-6}$ m/s).
- The standard deviation of the depth data errors are a specified percentage of the average value of h. The value used for the average is $h \approx \frac{c^2}{g} \approx \frac{1}{10} = 0.10$ m.
- The standard deviation of the longitude and latitude data errors are a specified percentage of size of the domain, which is $2^\circ \times 2^\circ$.

The specified percentages used for the errors in the initial conditions, dynamics and data in each twin experiment are given in Table 1

Experiment #	initial condition errors(% position and velocity)	model errors (% accelerations)	data errors (% depth and domain)
1	10.0	40.0	10.0
2	0.01	0.1	20.0
3	1.0	1.0	10.0

Table 1: Percentages used to estimate the standard deviation of errors in initial conditions, dynamics and data.

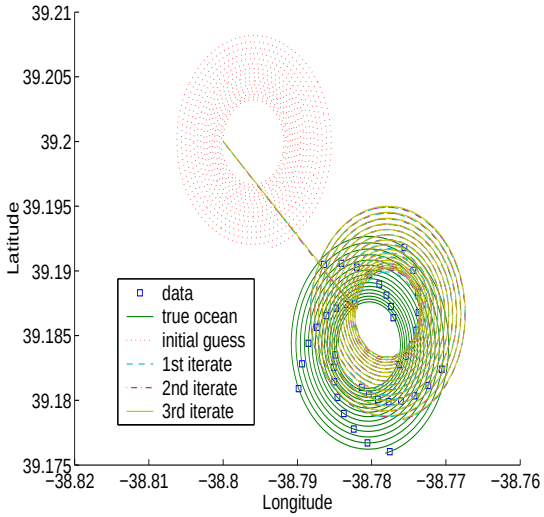

Figure 6: Assimilation results from experiment 1 in Table 1: one float with data recorded every eight hours.

The results from experiment 1 are in Figure 6. There we see that the first, second and third iterations are almost identical and they move from the initial guess to a trajectory near the true ocean. These choice of weights result in a good fit of the model and data on this particle.

The results from experiment 2 are in Figure 7. In this experiment it was assumed that the errors in the model and initial conditions were small, thus the 1st-3rd iterates to not move far from the initial guess. In addition, the data errors were specified larger than in experiment 1, thus in this experiment the model has more influence over the solution than the data.

In Figure 8 the results from experiment 3 are plotted. The specified errors in the initial condition and model are greater than in experiment 2 but less than in experiment 1, while the specified data errors are the same as in experiment 1. The trajectories move towards the true ocean since the data error is small, however, the error in the model is also assumed small, thus the assimilated trajectory stays closer to the initial guess than the assimilated trajectory in experiment 1.

Results in Figures 6-8 show the effect of different weights on the errors in the model and data. As we change the values of the weights, the inverse Lagrangian shallow water model reacts appropriately. The best choice of weights appears to be experiment 1, however, we will see in the next section that the results from particles for which there are no data are poor.

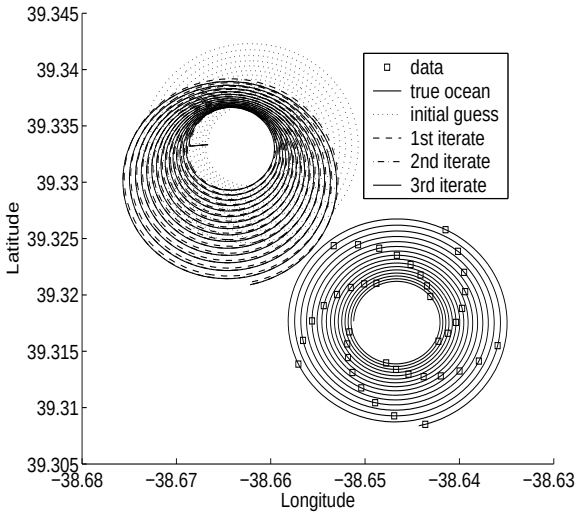

Figure 7: Assimilation results from experiment 2 in Table 1: one float with data recorded every eight hours.

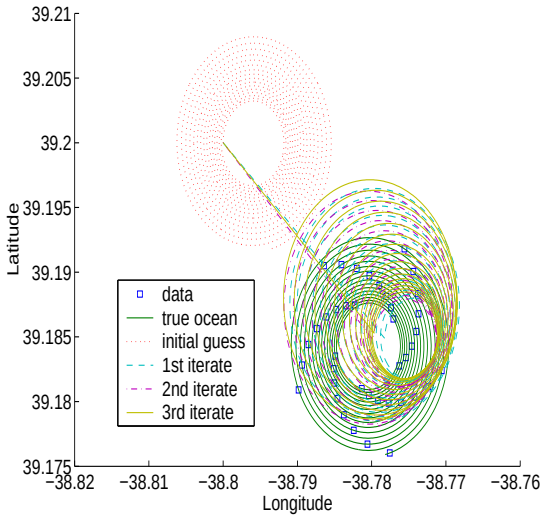

Figure 8: Assimilation results from experiment 3 in Table 1: one float with data recorded every eight hours.

4.2.1 Sampling of simulated data

In this section we study the effects of different spatial and temporal samplings of data.

Spatial sampling

In experiments 1-3 simulated float data were recorded for only one of the 4 x 4 particles, and data assimilation results from only that particle for which there are data are shown in Figures 6-8. This does not illustrate what occurs in the entire domain. In Figure 9(a) we do show results on the entire domain from experiment 1 when data are recorded at only particle 11. We do not clearly see the data, true ocean, or 3rd iterate in Figure 9(a), but the particles are numbered there for reference, and we can see that data is only recorded at particle 11. By looking more closely at some of the particles in Figure 9(b), one can see that particles 7 and 10 behave similarly (particle 10 is shown clearly in Figure 9(d)), while particle 11 and 6 are different from the others. A clear graph of particle 11 (where data are recorded) is plotted in Figure 6. On the other hand, a clear view of particle 6, where we have no data, is given in Figure 9(c). There, the trajectories from the iterations try to approach the true ocean, but they have no local data to guide them. It is interesting to note that data assimilated at particle 11 did not affect particle 10 or 7, but it did significantly affect particle 6. Thus our good assimilation result in Figure 6 is not true for all particles in the domain.

A better representation of the true ocean on the entire domain occurs when we increase the spatial sampling. In Figure 10 we show results when data from every other float were recorded (i.e. from eight floats). In Figure 10(a) there is not a clear view of the trajectories, but one can see that data are recorded at particles $1, 3, 6, 8, \ldots$. By looking at the particles more closely in Figure 10(b) we see that particles 7 and 10 behave similarly, while 6 and 11 behave similarly. There is a pattern where every float for which there are data has iterations that behave like particle 6 in Figure 10(c), while trajectories from those particles for which we have no data remain at their initial guess, and do not change, as particle 10 does in 10(d). Since the spatial sampling is dense in this experiment, we do not have the poor situation that occurred in Figure 9(c), where the trajectories move without ample guidance from data.

The pattern of the assimilated trajectories just described is a result of both the numerical approximation and the choice of diagonal weights. The spatial approximation is from a second order finite difference method and every other spatial grid point is used in the

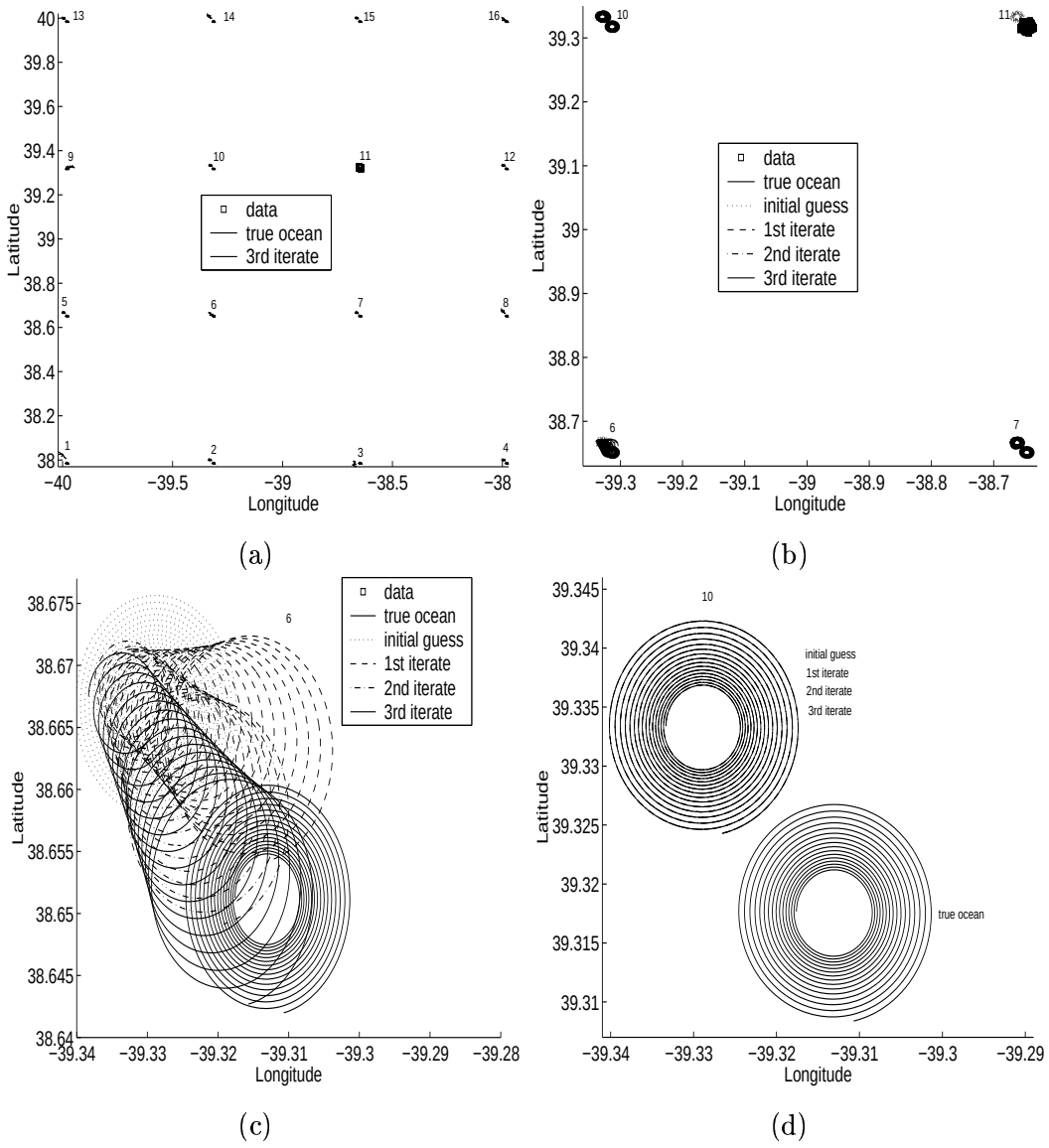

Figure 9: Assimilation results from experiment 1 in Table 1 with data recorded every eight hours at particle 11: all particles (a), four particles (b), particle 6 (c), and particle 10 (d).

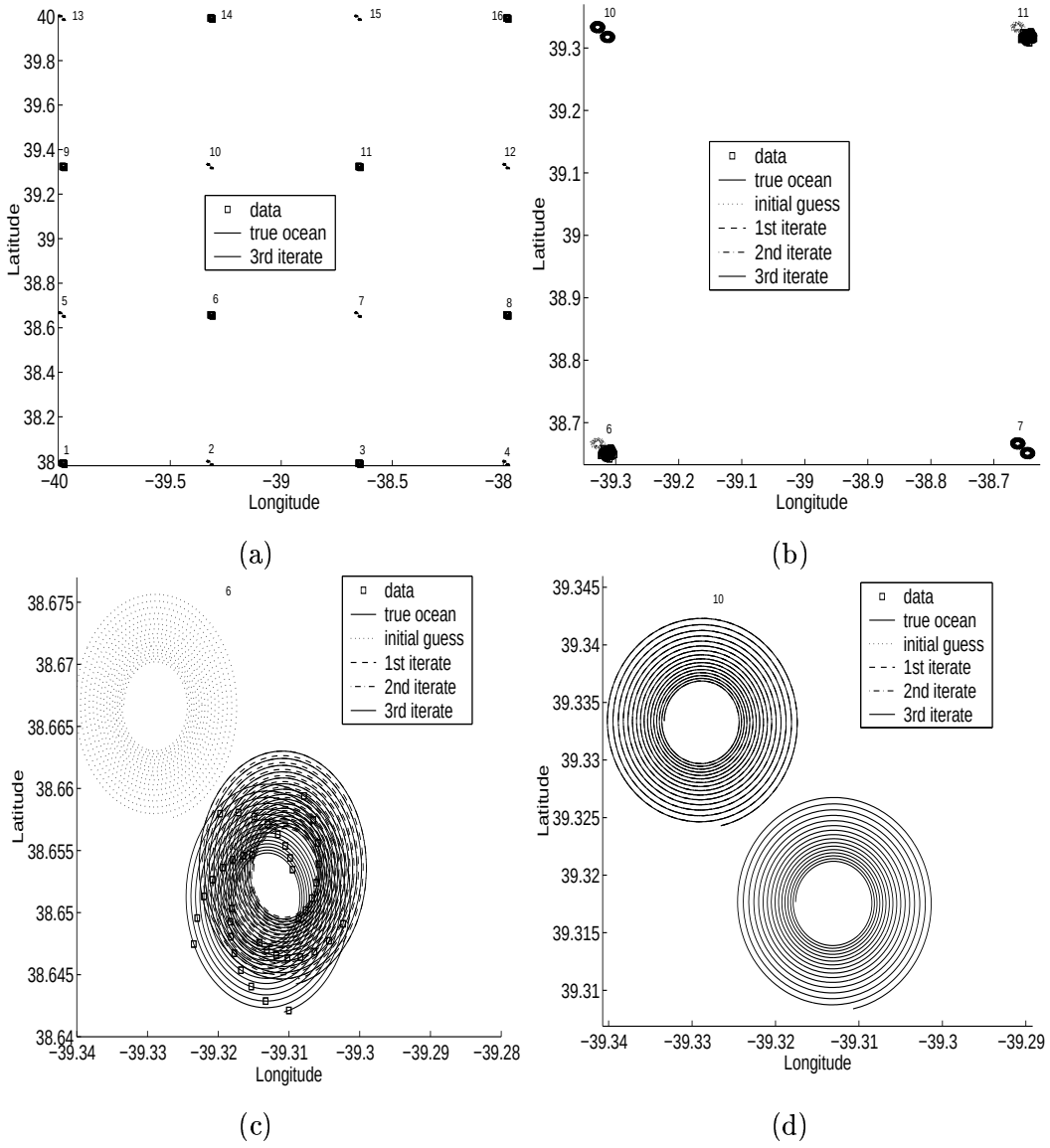

Figure 10: Assimilation results from experiment 1 in Table 1 with data recorded every eight hours at particles 1, 3, 6, 8, 9, 11, 14, and 16: all particles (a), four particles (b), particle 6 (c), and particle 10 (d).

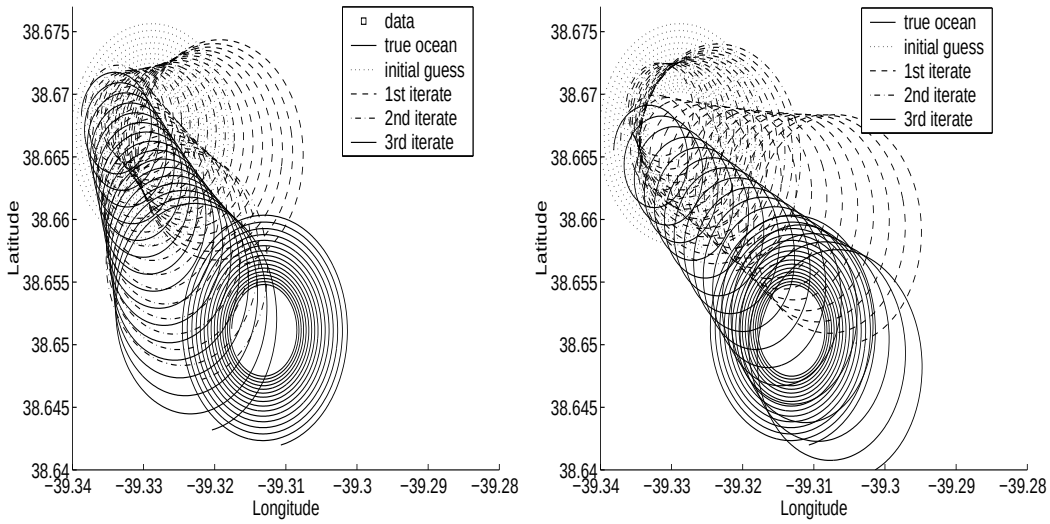

Figure 11: Assimilation results from experiment 1 in Table 1 with data at particle 11: particle 6 with data at particle 11 recorded every four hours (left) and 16 hours (right).

approximation. Thus spatial points are not affected by their neighbors. In addition, the choice of diagonal weighting results in no correlation of errors, thus errors at one spatial point will not affect its neighbors.

In experiment 2 when data are recorded only at particle 11 the 1st-3rd iterates remain at the initial guess on all other particles. On the other hand, in experiment 3 when data are recorded only at particle 11 we do have the poor situation that occurs in experiment 1. This can be remedied by increasing the spatial sampling or by reducing the weights on the errors in the initial conditions and model.

Temporal sampling

In the previous assimilations the simulated float data were recorded every 8 hours. Here, we in addition invert simulated data recorded every 4 and every 16 hours. The period of rotation of the particles changes with time, but there is roughly one oscillation per day in the first 13 days.

The significance of changing the temporal sampling is not seen at the one particle from which there are data, but at the other particles. In Figure 11 we plot assimilation results from particle 6 when data is recorded every 4 and 16 hours at particle 11. Compare this with Figure 9(c) where the result is from the same experiment but with data recorded at particle 11 every 8 hours. When we compare these three pictures we see that the trajec-

tories move past the true ocean as the data become less frequent temporally. However, the poor situation that occurs in Figure 9(c) is not remedied by increasing the temporal sampling.

In the case where there is dense spatial sampling, i.e. as in Figure 10 where data are recorded at every other particle, there is no significant change in assimilation results as the temporal sampling changes. Since with sparse spatial sampling the assimilation results do change as temporal sampling changes, this suggests that the optimal temporal sampling period is a function of the spatial sampling. Our results do not conflict with the optimal temporal sampling suggested in [11], rather we suggest that we should consider the temporal sampling in conjunction with the spatial sampling.

5 Conclusions

We have assimilated simulated float data directly into the viscous shallow water equations in Lagrangian coordinates. Using Lagrangian coordinates for the shallow water equations results in a highly nonlinear model. However, using the notation introduced in Appendices A-C it is fairly straightforward, but tedious, to linearize the equations and find the inverse. The forward nonlinear Lagrangian shallow water equations were integrated successfully for 100 days assuming phase speeds of 1 m/s and deformation radius of 35 km. With the same assumptions, and due to computational issues, the linearized model was successfully iterated for 25 days, and data successfully assimilated for 13 days.

The Lagrangian inverse model was tested by adjusting weights on the errors in the data and the dynamics, and the model behaved as dictated by the weights. Good fit of data and model was found with the choice of weights in experiment 1. However, when the Lagrangian trajectory data are sparse and the weight on the model errors is large, results from the assimilation may give a good representation of the true ocean on that trajectory, but a poor representation may result on other trajectories in the domain. If the spatial sampling is dense then there is no longer a poor representation of the true ocean at any point in the domain. Thus increasing the spatial sampling improved the assimilation results. In realistic situations, the data coverage may be poor and increasing the spatial sampling may not be an option. This means that we must rely heavily on the model and specify that the weights on the error in the model are small, as in experiment 2.

We varied the temporal sampling by recording trajectory position and depth every 4, 8 or 16 hours. These choices fall within the range of optimal samplings for the ocean surface specified in

[11]. When the spatial sampling was dense, this variation of temporal sampling did not effect the assimilation results. On the other hand, when the spatial sampling was sparse the variation did change the assimilation results. However, the assimilation results did not necessarily improve as the data became temporally more frequent.

These results show that Lagrangian coordinates can be used to assimilate Lagrangian data. However, these experiments were all done in an idealized environment. In order to use real data some significant improvements will need to be made. Firstly, the assumption of a flat earth must be eliminated, which means that the viscous terms may become too cumbersome for an exact representation in Lagrangian coordinates. Secondly, open boundary conditions must be developed and applied. An analysis must be done to determine the type and number of boundary conditions for the viscous Lagrangian equations. Then for long simulations absorbing or non-reflecting boundaries will be needed to used. Lastly, the implementation must be made more efficient, using some of the techniques in [5] such as accelerating the representer calculation and using it in parallel.

Acknowledgments

I am grateful to Andrew F. Bennett for helpful discussions and support.

Appendix A

Given an initial guess u^0 of the nonlinear solution of

$$\frac{\partial u}{\partial t} + u\frac{\partial u}{\partial x} = F, \tag{22}$$

its tangent linear form is

$$\frac{\partial u^n}{\partial t} + u^{n-1}\frac{\partial u^n}{\partial x} + (u^n - u^{n-1})\frac{\partial u^{n-1}}{\partial x} \quad = \quad F^{n-1}. \tag{23}$$

The nonlinearities in (22) can be simulated by iterating (23). When the model has many terms, it becomes convenient to write the linear form (23) as

$$\frac{\partial u^n}{\partial t} = k_1^{n-1}\frac{\partial u^n}{\partial x} + k_2^{n-1}u^n + k_3^{n-1}, \tag{24}$$

where

$$k_1^{n-1} \quad = \quad -u^{n-1} \tag{25}$$

$$k_2^{n-1} \quad = \quad -\frac{\partial u^{n-1}}{\partial x} \tag{26}$$

$$k_3^{n-1} \quad = \quad u^{n-1}\frac{\partial u^{n-1}}{\partial x} + F^{n-1} \tag{27}$$

are coefficients whose values are known at the nth iteration.

The tangent linear form of the viscid, Lagrangian shallow water model (5)-(7) has a significant number of terms (equation (5) alone has 21 terms!). We simplified the tangent linear form by using the exact solution of (7) and substituting J^{-1} with h/h_0. Using the above notation, the tangent linear form of the momentum equation for λ (5) is

$$\frac{\partial^2 \lambda^n}{\partial t^2} = \sum_{i=0}^{2}\sum_{j=0}^{2}\sum_{p=0}^{1}\left(k_{ijp}^{n-1}\frac{\partial^{(i+j+p)}}{\partial\alpha^i\beta^j t^p}\lambda^n + l_{ijp}^{n-1}\frac{\partial^{(i+j+p)}}{\partial\alpha^i\beta^j t^p}\theta^n + m_{ij}^{n-1}\frac{\partial^{(i+j)}}{\partial\alpha^i\beta^j}h^n \right) + c_\lambda^{n-1}, \quad (28)$$

The linearization of the momentum equation for θ (6) follows similarly, i.e.

$$\frac{\partial^2 \theta^n}{\partial t^2} = \sum_{i=0}^{2}\sum_{j=0}^{2}\sum_{p=0}^{1}\left(\hat{k}_{ijp}^{n-1}\frac{\partial^{(i+j+p)}}{\partial\alpha^i\beta^j t^p}\lambda^n + \hat{l}_{ijp}^{n-1}\frac{\partial^{(i+j+p)}}{\partial\alpha^i\beta^j t^p}\theta^n + \hat{m}_{ij}^{n-1}\frac{\partial^{(i+j)}}{\partial\alpha^i\beta^j}h^n \right) + c_\theta^{n-1}. \quad (29)$$

We solve the continuity equation (7) exactly, and its linear form is

$$h^n = \sum_{i=0}^{1}\sum_{j=0}^{1}\left(\bar{k}_{ij}^{n-1}\frac{\partial^{(i+j)}}{\partial\alpha^i\beta^j}\lambda^n + \bar{l}_{ij}^{n-1}\frac{\partial^{(i+j)}}{\partial\alpha^i\beta^j}\theta^n \right) + c_h^{n-1}. \quad (30)$$

The values of the coefficients k_{ijp}^{n-1}, l_{ijp}^{n-1}, m_{ij}^{n-1}, c_λ^{n-1}, $\hat{k}_{ijp}^{n-1}$, $\hat{l}_{ijp}^{n-1}$, $\hat{m}_{ij}^{n-1}$, c_θ^{n-1}, $\bar{k}_{ij}^{n-1}$, $\bar{l}_{ij}^{n-1}$, and c_h^{n-1} are given in Appendix B.

Appendix B

The values of the terms in the linearized viscid, Lagrangian shallow water model (28)-(30) on a flat earth are given in Tables 2-6. In order to simplify the presentation, we omit the superscript $^{n-1}$, and denote partial derivatives with subscripts, i.e.

$$\frac{\partial \lambda^{n-1}}{\partial t} = \lambda_t.$$

i	j	p	k_{ijp}	$\hat{k}_{ijp}$
0	0	0	0	0
0	0	1	$(\tan\theta_0)\,\theta_t$	$-\sin\theta_0\cos\theta_0(2\lambda_t+2\Omega)$
0	1	0	$-\frac{\kappa}{r^2}\left(\frac{h}{h_0}\right)^2\left(\frac{\partial(\lambda_\alpha,\lambda_t)}{\partial(\alpha,\beta)}+2\frac{\partial(\lambda,\lambda_{t\alpha})}{\partial(\alpha,\beta)}\right)$	$-\frac{\kappa}{r^2}\left(\frac{h}{h_0}\right)^2\left(\frac{\partial(\lambda_\alpha,\theta_t)}{\partial(\alpha,\beta)}+2\frac{\partial(\lambda,\theta_{t\alpha})}{\partial(\alpha,\beta)}\right)+\frac{g}{r^2}\frac{h}{h_0}h_\alpha$
0	1	1	$\frac{\kappa}{r^2}\left(\frac{h}{h_0}\right)^2\left(\frac{1}{\cos^2\theta_0}\frac{\partial(\theta,\theta_\alpha)}{\partial(\alpha,\beta)}+\frac{\partial(\lambda,\lambda_\alpha)}{\partial(\alpha,\beta)}\right)$	0
0	2	0	$-\frac{\kappa}{r^2}\left(\frac{h}{h_0}\right)^2\lambda_\alpha\lambda_{t\alpha}$	$-\frac{\kappa}{r^2}\left(\frac{h}{h_0}\right)^2\lambda_\alpha\theta_{t\alpha}$
0	2	1	$\frac{\kappa}{r^2}\left(\frac{h}{h_0}\right)^2\left(\frac{1}{\cos^2\theta_0}\theta_\alpha^2+\lambda_\alpha^2\right)$	0
1	0	0	$\frac{\kappa}{r^2}\left(\frac{h}{h_0}\right)^2\left(\frac{\partial(\lambda_\beta,\lambda_t)}{\partial(\alpha,\beta)}+2\frac{\partial(\lambda,\lambda_{t\beta})}{\partial(\alpha,\beta)}\right)$	$\frac{\kappa}{r^2}\left(\frac{h}{h_0}\right)^2\left(\frac{\partial(\lambda_\beta,\theta_t)}{\partial(\alpha,\beta)}+2\frac{\partial(\lambda,\theta_{t\beta})}{\partial(\alpha,\beta)}\right)-\frac{g}{r^2}\frac{h}{h_0}h_\beta$
1	0	1	$\frac{\kappa}{r^2}\left(\frac{h}{h_0}\right)^2\left(\frac{1}{\cos^2\theta_0}\frac{\partial(\theta_\beta,\theta)}{\partial(\alpha,\beta)}+\frac{\partial(\lambda_\beta,\lambda)}{\partial(\alpha,\beta)}\right)$	0
1	1	0	$\frac{\kappa}{r^2}\left(\frac{h}{h_0}\right)^2(\lambda_\alpha\lambda_{t\beta}+\lambda_\beta\lambda_{t\alpha})$	$\frac{\kappa}{r^2}\left(\frac{h}{h_0}\right)^2(\lambda_\alpha\theta_{t\beta}+\lambda_\beta\theta_{t\alpha})$
1	1	1	$-2\frac{\kappa}{r^2}\left(\frac{h}{h_0}\right)^2\left(\frac{1}{\cos^2\theta_0}\theta_\alpha\theta_\beta+\lambda_\alpha\lambda_\beta\right)$	0
1	2	0	0	0
1	2	1	0	0
2	0	0	$-\frac{\kappa}{r^2}\left(\frac{h}{h_0}\right)^2\lambda_\beta\lambda_{t\beta}$	$-\frac{\kappa}{r^2}\left(\frac{h}{h_0}\right)^2\lambda_\beta\theta_{t\beta}$
2	0	1	$\frac{\kappa}{r^2}\left(\frac{h}{h_0}\right)^2\left(\frac{1}{\cos^2\theta_0}\theta_\beta^2+\lambda_\beta^2\right)$	0
2	1	0	0	0
2	1	1	0	0

Table 2: Values for k_{ijp} and $\hat{k_{ijp}}$.

i	j	p	l_{ijp}	$\hat{l}_{ijp}$
0	0	0	0	
0	0	1	$\tan\theta_0(\lambda_t + 2\Omega)$	0
0	1	0	$\frac{\kappa}{r^2\cos^2\theta_0}\left(\frac{h}{h_0}\right)^2\left(\frac{\partial(\lambda_t,\theta_\alpha)}{\partial(\alpha,\beta)} + 2\frac{\partial(\lambda_{t\alpha},\theta)}{\partial(\alpha,\beta)}\right) - \frac{g}{r^2\cos^2\theta_0}\frac{h}{h_0}h_\alpha$	$\frac{\kappa}{r^2\cos^2\theta_0}\left(\frac{h}{h_0}\right)^2\left(\frac{\partial(\theta_t,\theta_\alpha)}{\partial(\alpha,\beta)} + 2\frac{\partial(\theta_{t\alpha},\theta)}{\partial(\alpha,\beta)}\right)$
0	1	1	0	$\frac{\kappa}{r^2}\left(\frac{h}{h_0}\right)^2\left(\frac{1}{\cos^2\theta_0}\frac{\partial(\theta,\theta_\alpha)}{\partial(\alpha,\beta)} + \frac{\partial(\lambda,\lambda_\alpha)}{\partial(\alpha,\beta)}\right)$
0	2	0	$-\frac{\kappa}{r^2\cos^2\theta_0}\left(\frac{h}{h_0}\right)^2\theta_\alpha\lambda_{t\alpha}$	$-\frac{\kappa}{r^2\cos^2\theta_0}\left(\frac{h}{h_0}\right)^2\theta_\alpha\theta_{t\alpha}$
0	2	1	0	$\frac{\kappa}{r^2}\left(\frac{h}{h_0}\right)^2\left(\frac{1}{\cos^2\theta_0}\theta_\alpha^2 + \lambda_\alpha^2\right)$
1	0	0	$-\frac{\kappa}{r^2\cos^2\theta_0}\left(\frac{h}{h_0}\right)^2\left(\frac{\partial(\lambda_t,\theta_\beta)}{\partial(\alpha,\beta)} + 2\frac{\partial(\lambda_{t\beta},\theta)}{\partial(\alpha,\beta)}\right) + \frac{g}{r^2\cos^2\theta_0}\frac{h}{h_0}h_\beta$	$-\frac{\kappa}{r^2\cos^2\theta_0}\left(\frac{h}{h_0}\right)^2\left(\frac{\partial(\theta_t,\theta_\beta)}{\partial(\alpha,\beta)} + 2\frac{\partial(\theta_{t\beta},\theta)}{\partial(\alpha,\beta)}\right)$
1	0	1	0	$\frac{\kappa}{r^2}\left(\frac{h}{h_0}\right)^2\left(\frac{1}{\cos^2\theta_0}\frac{\partial(\theta_\beta,\theta)}{\partial(\alpha,\beta)} + \frac{\partial(\lambda_\beta,\lambda)}{\partial(\alpha,\beta)}\right)$
1	1	0	$\frac{\kappa}{r^2\cos^2\theta_0}\left(\frac{h}{h_0}\right)^2(\theta_\alpha\lambda_{t\beta} + \theta_\beta\lambda_{t\alpha})$	$\frac{\kappa}{r^2\cos^2\theta_0}\left(\frac{h}{h_0}\right)^2(\theta_\alpha\theta_{t\beta} + \theta_\beta\theta_{t\alpha})$
1	1	1	0	$-2\frac{\kappa}{r^2}\left(\frac{h}{h_0}\right)^2\left(\frac{1}{\cos^2\theta_0}\theta_\alpha\theta_\beta + \lambda_\alpha\lambda_\beta\right)$
1	2	0	0	0
1	2	1	0	0
2	0	0	$-\frac{\kappa}{r^2\cos^2\theta_0}\left(\frac{h}{h_0}\right)^2\theta_\beta\lambda_{t\beta}$	$-\frac{\kappa}{r^2\cos^2\theta_0}\left(\frac{h}{h_0}\right)^2\theta_\beta\theta_{t\beta}$
2	0	1	0	$\frac{\kappa}{r^2}\left(\frac{h}{h_0}\right)^2\left(\frac{1}{\cos^2\theta_0}\theta_\beta^2 + \lambda_\beta^2\right)$
2	1	0	0	0
2	1	1	0	0

Table 3: Values for l_{ijp} and $\hat{l_{ijp}}$.

i	j	m_{ij}	$\hat{m}_{ij}$
0	0	$-\frac{g}{r^2\cos^2\theta_0 h_0}\frac{\partial(h,\theta)}{\partial(\alpha,\beta)} + \frac{2\kappa}{r^2 h_0}\left(\frac{1}{\cos^2\theta_0}\frac{\partial(L,\theta)}{\partial(\alpha,\beta)} + \frac{\partial(\lambda,M)}{\partial(\alpha,\beta)}\right)$	$-\frac{g}{r^2 h_0}\frac{\partial(\lambda,h)}{\partial(\alpha,\beta)} + \frac{2\kappa}{r^2 h_0}\left(\frac{1}{\cos^2\theta_0}\frac{\partial(N,\theta)}{\partial(\alpha,\beta)} + \frac{\partial(\lambda,O)}{\partial(\alpha,\beta)}\right)$
0	1	$\frac{g}{r^2\cos^2\theta_0}\left(\frac{h}{h_0}\right)\theta_\alpha$	$-\frac{g}{r^2}\left(\frac{h}{h_0}\right)\lambda_\alpha$
1	0	$-\frac{g}{r^2\cos^2\theta_0}\left(\frac{h}{h_0}\right)\theta_\beta$	$\frac{g}{r^2}\left(\frac{h}{h_0}\right)\lambda_\beta$

Table 4: Values for m_{ijp} and $\hat{m_{ijp}}$.

c_λ
$-\tan\theta_0\lambda_t\theta_t + \frac{h}{r^2 h_0}\left(\frac{2g}{\cos^2\theta_0}\frac{\partial(h,\theta)}{\partial(\alpha,\beta)} - 4\kappa\left(\frac{1}{\cos^2\theta_0}\frac{\partial(L,\theta)}{\partial(\alpha,\beta)} + \frac{\partial(\lambda,M)}{\partial(\alpha,\beta)}\right)\right)$

c_θ
$\sin\theta_0\cos\theta_0\lambda_t^2 + \frac{h}{r^2 h_0}\left(\frac{2g}{\cos^2\theta_0}\frac{\partial(\lambda,h)}{\partial(\alpha,\beta)} - 4\kappa\left(\frac{1}{\cos^2\theta_0}\frac{\partial(N,\theta)}{\partial(\alpha,\beta)} + \frac{\partial(\lambda,O)}{\partial(\alpha,\beta)}\right)\right)$

Table 5: Values for c_λ and c_θ.

i	j	$\bar{k}_{ij}$	$\bar{l}_{ij}$	c_h
0	0	0	0	
0	1	$\frac{h^2}{h_0}\theta_\alpha$	$-\frac{h^2}{h_0}\lambda_\alpha$	
1	0	$-\frac{h^2}{h_0}\theta_\beta$	$\frac{h^2}{h_0}\lambda_\beta$	
				$3h$

Table 6: Values for $\bar{k_{ij}}$ and $\bar{l_{ij}}$.

Appendix C

The Euler-Lagrange equations are a coupled two-point initial boundary problem consisting of a set of backward and forward equations. In order to simplify the presentation we will neglect the $^{n-1}$ superscripts and state the equations for any given iterate. The minimum of the penalty functional $\mathcal{J}$ occurs at $\hat{\lambda}$, $\hat{\theta}$, and $\hat{h}$ and these values can be found by solving the Euler-Lagrange equations which also include the following adjoint variables ξ^λ and ξ^θ:

$$\begin{aligned}
\xi^\lambda &= \int_0^T dt \int_{\alpha_w}^{\alpha_e} d\alpha \int_{\beta_s}^{\beta_n} d\beta W_{f_\lambda} f_\lambda \\
\xi^\theta &= \int_0^T dt \int_{\alpha_w}^{\alpha_e} d\alpha \int_{\beta_s}^{\beta_n} d\beta W_{f_\lambda} f_\theta .
\end{aligned}$$

Let γ be the Lagrange multiplier used for constraining the equation for h (15). Then the backward Euler-Lagrange equations are

$$\begin{aligned}
\frac{\partial^2 \xi^\lambda}{\partial t^2} &= \sum_{i=0}^{2}\sum_{j=0}^{2}\sum_{p=0}^{1}\left((-1)^{i+j+p} k_{ijp} \frac{\partial^{(i+j+p)}}{\partial \alpha^i \beta^j t^p} \xi^\lambda + (-1)^{i+j+p} \hat{k}_{ijp} \frac{\partial^{(i+j+p)}}{\partial \alpha^i \beta^j t^p} \xi^\theta + (-1)^{i+j} \bar{k}_{ij} \frac{\partial^{(i+j)}}{\partial \alpha^i \beta^j} \gamma \right) \\
&\quad + \omega_\lambda \sum_{m=1}^{M} \delta(\alpha - \alpha_m)\delta(\beta - \beta_m)\delta(t - t_m) \left(d_m^\lambda - \hat{\lambda}(\alpha_m, \beta_m, t_m) \right) \qquad (31) \\
\frac{\partial^2 \xi^\theta}{\partial t^2} &= \sum_{i=0}^{2}\sum_{j=0}^{2}\sum_{p=0}^{1}\left((-1)^{i+j+p} l_{ijp} \frac{\partial^{(i+j+p)}}{\partial \alpha^i \beta^j t^p} \xi^\lambda + (-1)^{i+j+p} \hat{l}_{ijp} \frac{\partial^{(i+j+p)}}{\partial \alpha^i \beta^j t^p} \xi^\theta + (-1)^{i+j} \bar{l}_{ij} \frac{\partial^{(i+j)}}{\partial \alpha^i \beta^j} \gamma \right) \\
&\quad + \omega_\theta \sum_{m=1}^{M} \delta(\alpha - \alpha_m)\delta(\beta - \beta_m)\delta(t - t_m) \left(d_m^\theta - \hat{\theta}(\alpha_m, \beta_m, t_m) \right) \qquad (32) \\
\gamma &= \sum_{i=0}^{2}\sum_{j=0}^{2}\left((-1)^{i+j} m_{ij} \frac{\partial^{(i+j)}}{\partial \alpha^i \beta^j} \xi^\lambda + (-1)^{i+j} \hat{m}_{ij} \frac{\partial^{(i+j)}}{\partial \alpha^i \beta^j} \xi^\theta \right) \\
&\quad + \omega_h \sum_{m=1}^{M} \delta(\alpha - \alpha_m)\delta(\beta - \beta_m)\delta(t - t_m) \left(d_m^h - \hat{h}(\alpha_m, \beta_m, t_m) \right) \qquad (33)
\end{aligned}$$

with terminal conditions

$$\begin{aligned}
\xi^\lambda(\alpha, \beta, T) &= \xi_t^\lambda(\alpha, \beta, T) = 0 \qquad (34) \\
\xi^\theta(\alpha, \beta, T) &= \xi_t^\theta(\alpha, \beta, T) = 0. \qquad (35)
\end{aligned}$$

The forward Euler-Lagrange equations are

$$\frac{\partial^2 \hat{\lambda}}{\partial t^2} = \sum_{i=0}^{2}\sum_{j=0}^{2}\sum_{p=0}^{1}\left(k_{ijp}\frac{\partial^{(i+j+p)}}{\partial\alpha^i\beta^j t^p}\hat{\lambda} + l_{ijp}\frac{\partial^{(i+j+p)}}{\partial\alpha^i\beta^j t^p}\hat{\theta} + m_{ij}\frac{\partial^{(i+j)}}{\partial\alpha^i\beta^j}\hat{h}\right) + c_\lambda^{n-1} + W_{f_\lambda}^{-1}\xi^\lambda \quad (36)$$

$$\frac{\partial^2 \hat{\theta}}{\partial t^2} = \sum_{i=0}^{2}\sum_{j=0}^{2}\sum_{p=0}^{1}\left(\hat{k}_{ijp}\frac{\partial^{(i+j+p)}}{\partial\alpha^i\beta^j t^p}\hat{\lambda} + \hat{l}_{ijp}\frac{\partial^{(i+j+p)}}{\partial\alpha^i\beta^j t^p}\hat{\theta} + \hat{m}_{ij}\frac{\partial^{(i+j)}}{\partial\alpha^i\beta^j}\hat{h}\right) + c_\theta + W_{f_\theta}^{-1}\xi^\theta \quad (37)$$

$$\hat{h} = \sum_{i=0}^{1}\sum_{j=0}^{1}\left(\bar{k}_{ij}\frac{\partial^{(i+j)}}{\partial\alpha^i\beta^j}\hat{\lambda} + \bar{l}_{ij}\frac{\partial^{(i+j)}}{\partial\alpha^i\beta^j}\hat{\theta}\right) + c_h \quad (38)$$

with initial conditions

$$\hat{\lambda}(\alpha,\beta,0) = \alpha - W_{i_\lambda}^{-1}\left\{\frac{\partial}{\partial t}\xi^\lambda(\alpha,\beta,0) + \sum_{i=0}^{2}\sum_{j=0}^{2}\left((-1)^{i+j}k_{ij}\frac{\partial^{(i+j)}}{\partial\alpha^i\beta^j}\xi^\lambda(\alpha,\beta,0) + (-1)^{i+j}\hat{k}_{ij}\frac{\partial^{(i+j)}}{\partial\alpha^i\beta^j}\xi^\theta(\alpha,\beta,0)\right)\right\} \quad (39)$$

$$\hat{\theta}(\alpha,\beta,0) = \beta - W_{i_\theta}^{-1}\left\{\frac{\partial}{\partial t}\xi^\theta(\alpha,\beta,0) + \sum_{i=0}^{2}\sum_{j=0}^{2}\left((-1)^{i+j}l_{ij}\frac{\partial^{(i+j)}}{\partial\alpha^i\beta^j}\xi^\lambda(\alpha,\beta,0) + (-1)^{i+j}\hat{l}_{ij}\frac{\partial^{(i+j)}}{\partial\alpha^i\beta^j}\xi^\theta(\alpha,\beta,0)\right)\right\}, \quad (40)$$

and

$$\frac{\partial}{\partial t}\hat{\lambda}(\alpha,\beta,0) = u^I + W_{i_{\lambda_t}}^{-1}\xi^\lambda(\alpha,\beta,0) \quad (41)$$

$$\frac{\partial}{\partial t}\hat{\theta}(\alpha,\beta,0) = v^I + W_{i_{\theta_t}}^{-1}\xi^\theta(\alpha,\beta,0) \quad (42)$$

$$h(\alpha,\beta,0) = h^I. \quad (43)$$

References

[1] Bennett, A. F., "Inverse Modelling of the Ocean and Atmosphere", Cambridge University Press, 234 pp., 2002.

[2] Bennett, A.F., and B.S. Chua, "Open Boundary Conditions for Lagrangian Geophysical Fluid Dynamics," *J. Comp. Phys.* **153**, pp. 418-436, 1999.

[3] Berger M.J., Oliger J., "Adaptive mesh refinement for hyperbolic partial differential equations", *J. Comp. Phys.*, **53**, pp. 484-512, 1984.

[4] Chelton, D.B., R.A. deSzoeke, and M.G. Schlax, "Geographical Variability of the First Baroclinic Rossby Radius of Deformation", *J. Phys. Oceanogr.,* Vol. 28, No. 3, pp. 433-460, 1998.

[5] Chua, B. S. and A. F. Bennett,"An Inverse Ocean Modelling System", *Ocean Modelling*, **3**, pp. 137-165, 2001.

[6] B. Engquist and A. Majda, "Absorbing Boundary Conditions for the Numerical Simulation of Waves", *Math. Comput.*, Vol. 31, No. 139, pp. 629-651, 1997

[7] Gill, A.E., "Atmosphere - Ocean Dynamics", Academic Press Inc., 662 pp., 1982.

[8] Kamachi, M. and J.J. O'Brien, "Continuous Data Assimilation of Drifting Buoy Trajectory into an Equatorial Pacific Ocean Model", *J. Mar. Sys.*, 6, pp. 159-178, 1995.

[9] Margolin, L., "Introduction to "Arbitrary Lagrangian-Eulerian Computing Method for All Flow Speeds", *J. Comp. Phys.*, 135, pp. 198-202, 1997.

[10] Mead, J.L. and Bennett, A.F., "Towards Regional Assimilation of Lagrangian Data: The Lagrangian form of the Shallow Water Reduced Gravity Model and its Inverse", *Journal of Marine Systems*, **29**, pp.365-384, 2001.

[11] Molcard, A., Piterbarg, L.I., Griffa, A., Özgökmen and Mariano, A.J., "Assimilation of Drifter Obervations for the Reconstruction of the Eulerian Circulation Field", *J. Geophys. Res. (oceans)*, Vol. 108, No. C3, 3056, doi:10.1029/2001JC001240, 2003.

[12] Noh, W.F. and Woodward, P., "Simple Line Interface Calculation", *Proceedings of the Fifth International Conference on Numerical Methods in Fluid Dynamics*, Berlin, 1976.

[13] Oliger, J., and A. Sundström, "Theoretical and practical aspects of some initial boundary value problems in fluid dynamics", *SIAM J. Appl. Math.,* **35**, pp. 419-446, 1978.

[14] S. Osher and J.A. Sethian, "Fronts propagating with curvature dependent speed: algorithms based on Hamilton-Jacobi formulations", *J. Comput. Phys.*, **79**, pp. 12-49, 1988.

[15] Staniforth, A. and Côteé, "Semi-Lagrangian Integration Schemes for Atmospheric Models - A Review", *Mon. Wea. Rev.* Vol. 119, pp. 2206-2080, 1991.

[16] Toner, M., Kirwan Jr., A.D., Kantha, L.H. and Choi, J.K, "Can General Circulation Models be Assessed and their Output Enhanced with Drifter Data?", *J. Geophys. Res. (oceans)*, Vol. 106, No. C9, pp. 19,563-19,579, 2001.

[17] Yang, J.-Y, Hsu, C.A. and Hui, W.H., "A Generalized Lagrangian method for solving the steady shallow water equations", *Math. Comput. Simul.* **35**, pp.43-61, 1993.